Supplement of Hydrol. Earth Syst. Sci., 28, 4455–4476, 2024
https://doi.org/10.5194/hess-28-4455-2024-supplement

Hydrology and Earth System Sciences
Open Access
EGU

Supplement of

Multi-objective calibration and evaluation of the ORCHIDEE land surface model over France at high resolution

Peng Huang et al.

Correspondence to: Peng Huang (peng.huang@sorbonne-universite.fr)

Supplement

S1 PFTs in the ORCHIDEE LSM

Table S1. Overview of the 15 PFTs used in ORCHIDEE with the root density value c of each PFT used for CMIP6 configuration (ref) and for this study (new). PFTs 2, 3, and 14 do not appear in France.

PFT	Description	c of ref [-]	c of new [-]
1	bare soil	5.0	5.0
2	tropical broadleaf evergreen	0.8	0.8
3	tropical broadleaf raingreen	0.8	0.8
4	temperate needleleaf evergreen	1.0	1.0
5	temperate broadleaf evergreen	0.8	0.8
6	temperate broadleaf summergreen	0.8	1.5
7	boreal needleleaf evergreen	1.0	2.0
8	boreal broadleaf summergreen	1.0	2.0
9	boreal needleleaf deciduous	0.8	1.5
10	temperate natural grassland (C3)	4.0	4.0
11	natural grassland (C4)	4.0	4.0
12	crops (C3)	4.0	2.0
13	crops (C4)	4.0	2.0
14	tropical natural grassland (C3)	4.0	4.0
15	boreal natural grassland (C3)	4.0	6.0

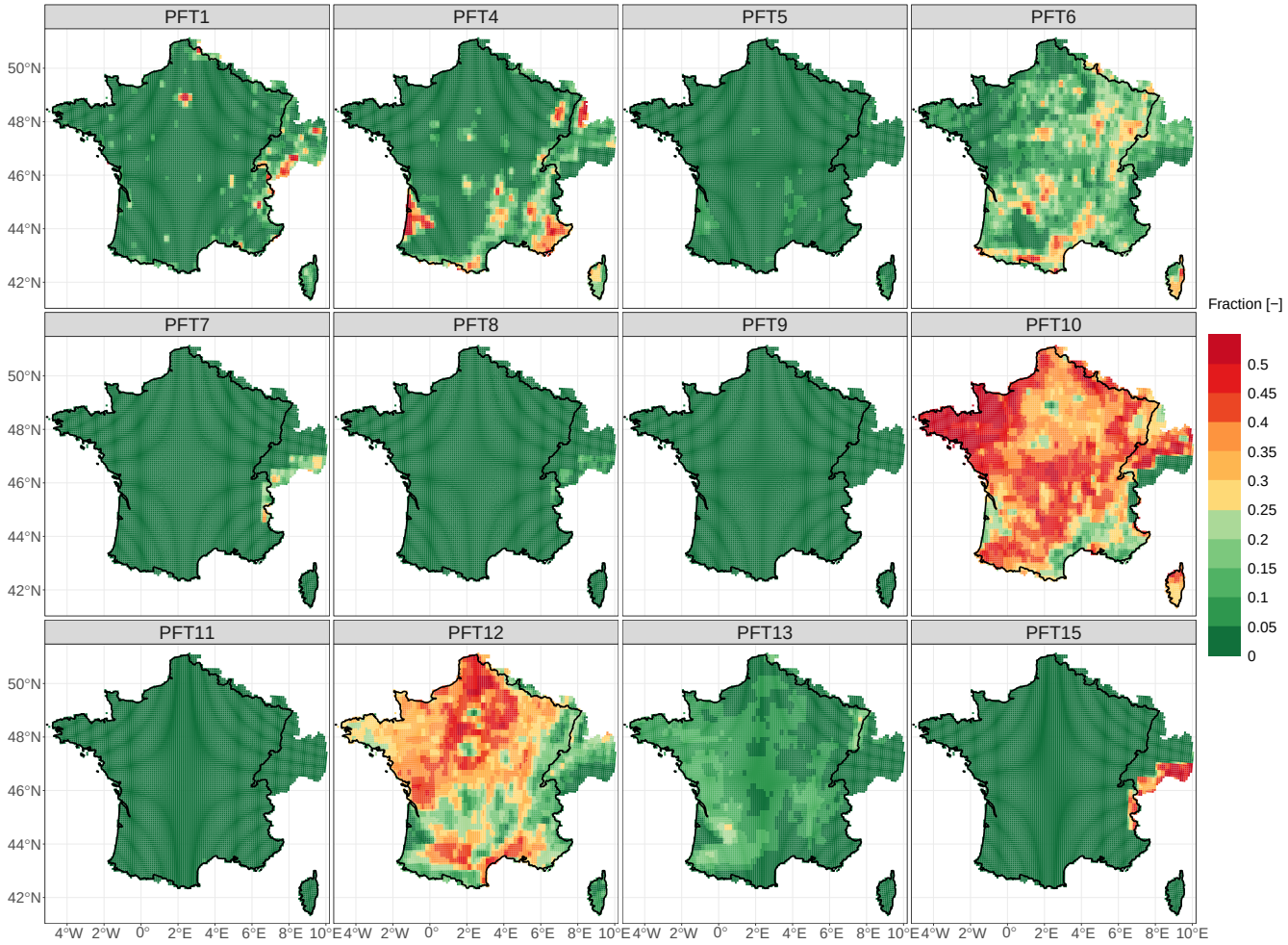

Figure S1. The spatial distribution of the PFTs that appear in France averaged over the 1959-2020 period based on the LUH2 dataset (Hurtt et al., 2020) reaggregated into Safran grid cells.

S2 The Reynolds soil texture map

Table S2. Overview of the 12 soil texture classes in the Reynolds soil texture map (Sa = sand, Si = silt, L = loam, and C = clay) (Reynolds et al., 2000), their reference hydraulic conductivity (K_s^{ref}) and their water retention properties (volumetric water content at saturation θ_s, field capacity θ_c and wilting point θ_w).

Index	1	2	3	4	5	6	7	8	9	10	11	12
Soil texture	Sa	LSa	SaL	SiL	Si	L	SaCL	SiCL	CL	SaC	SiC	C
K_s^{ref} [mm/d]	7128.0	3501.6	1060.8	108.0	60.0	249.6	314.4	16.8	62.4	28.8	4.8	48.0
θ_s [m^3/m^3]	0.43	0.41	0.41	0.45	0.46	0.43	0.39	0.43	0.41	0.38	0.36	0.38
θ_c [m^3/m^3]	0.0493	0.0710	0.1218	0.2402	0.2582	0.1654	0.1695	0.3383	0.2697	0.2672	0.3370	0.3469
θ_w [m^3/m^3]	0.0450	0.0570	0.0657	0.1039	0.0901	0.0884	0.1112	0.1967	0.1496	0.1704	0.2665	0.2707

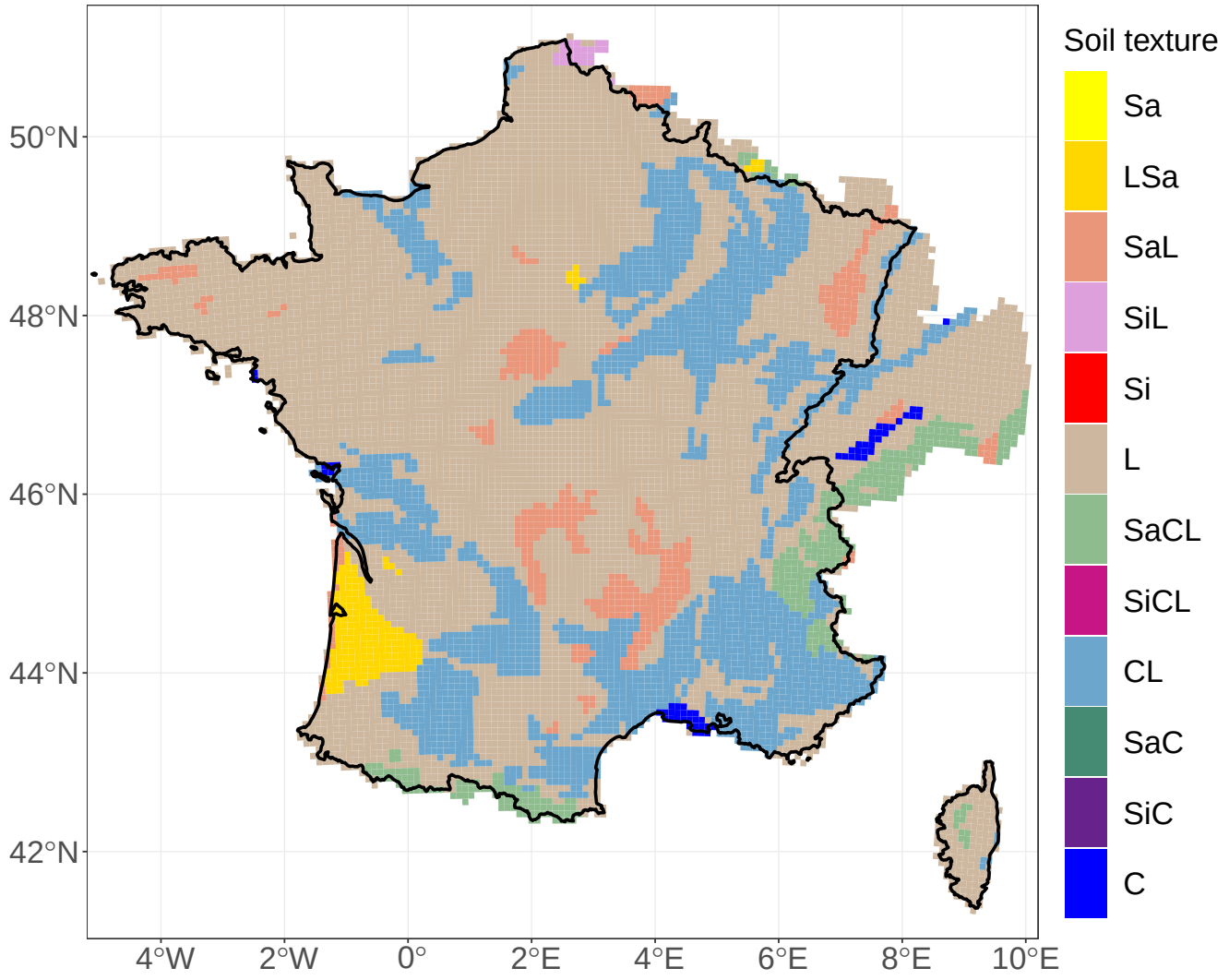

Figure S2. The dominant soil texture classes in France based on the Reynolds soil texture map (Reynolds et al., 2000) reaggregated into Safran grid cells.

S3 Calibration of roughness length parameters

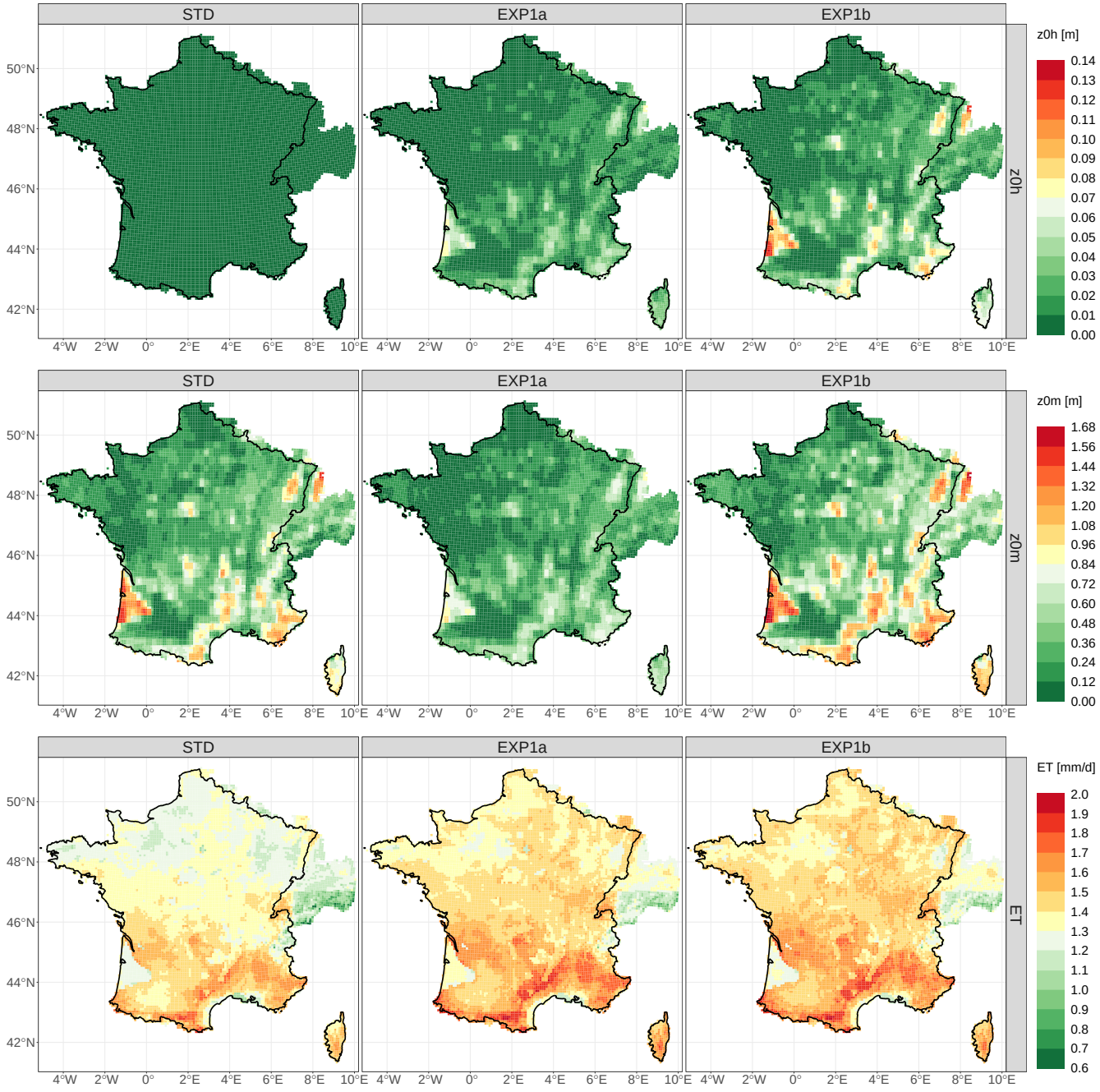

Figure S3. The spatial distributions of the simulated z_{0h}, z_{0m}, and ET values averaged over the 1959-2020 period in France for the calibration experiments STD, EXP1a, and EXP1b.

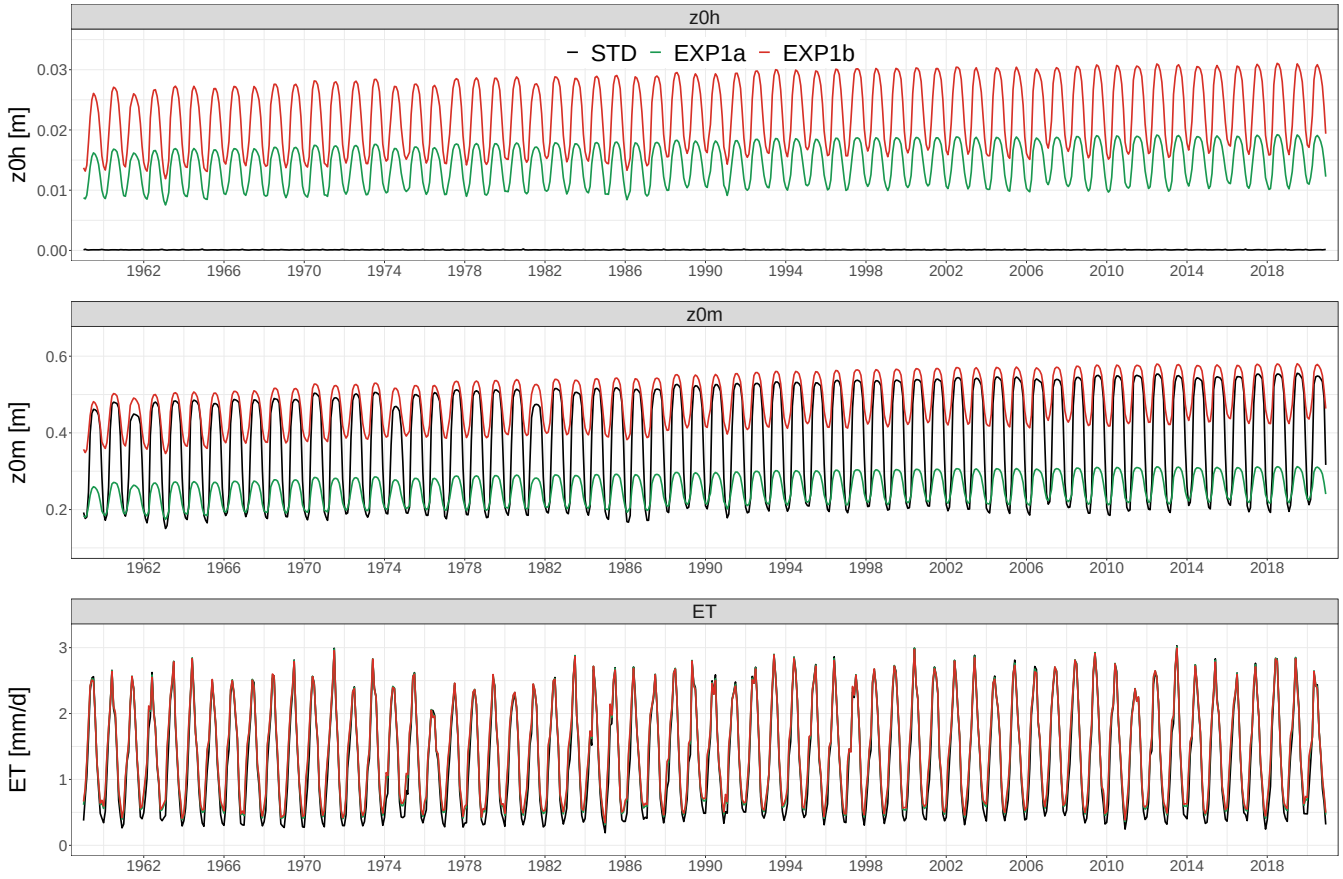

Figure S4. The time series of the simulated z_{0h}, z_{0m}, and ET values averaged over France from 1959 to 2020 for the calibration experiments STD, EXP1a, and EXP1b.

S4 Calibration of soil hydraulic conductivity

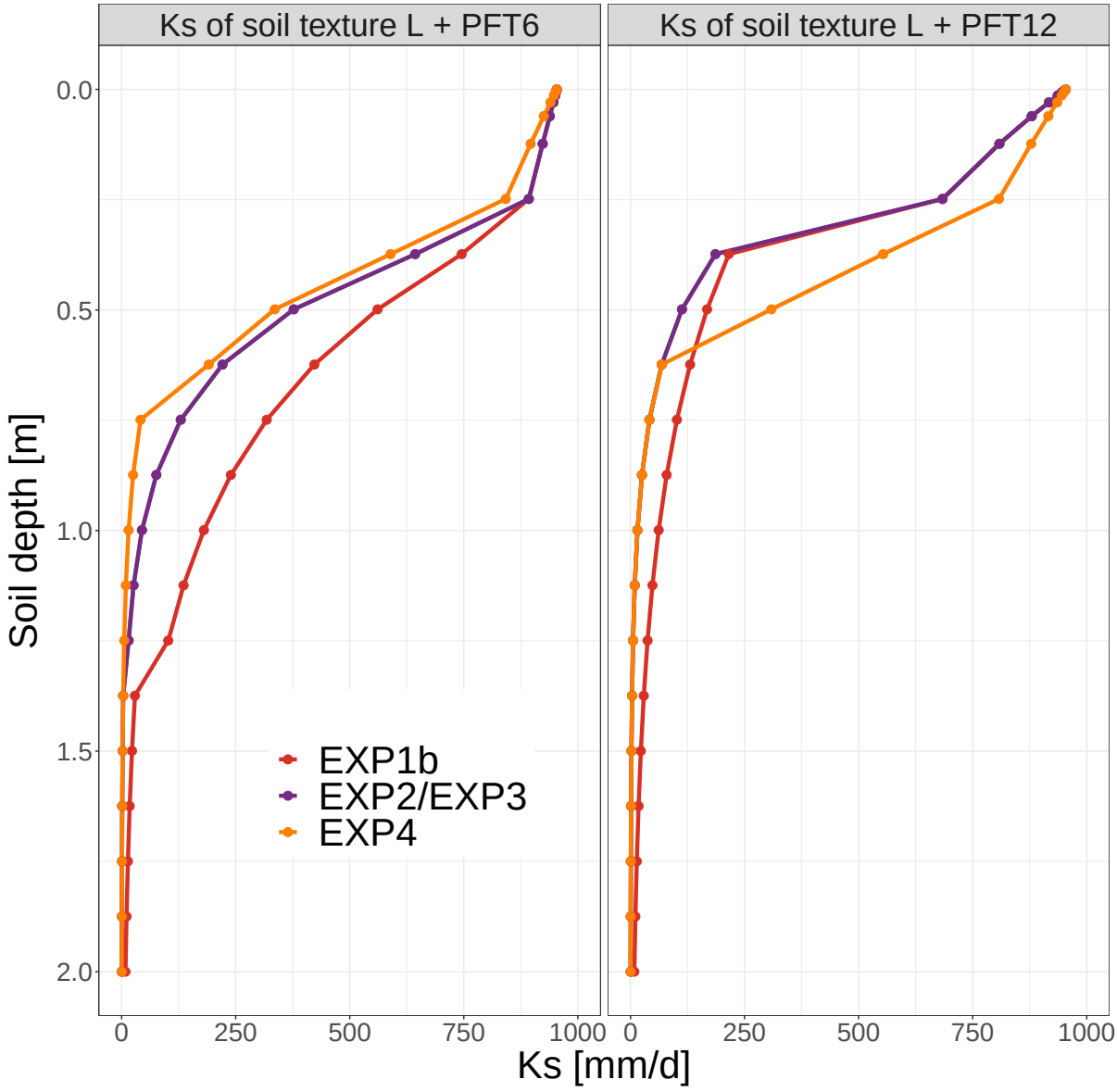

Figure S5. Two examples showing how soil hydraulic conductivity is impacted by soil compaction (an exponential decrease with depth) and vegetal roots (an increase towards the soil surface): the loamy soil class (L) covered by trees (PFT6) in the left and by crops (PFT12) on the right for the calibration experiments EXP1b, EXP2 (or EXP3), and EXP4.

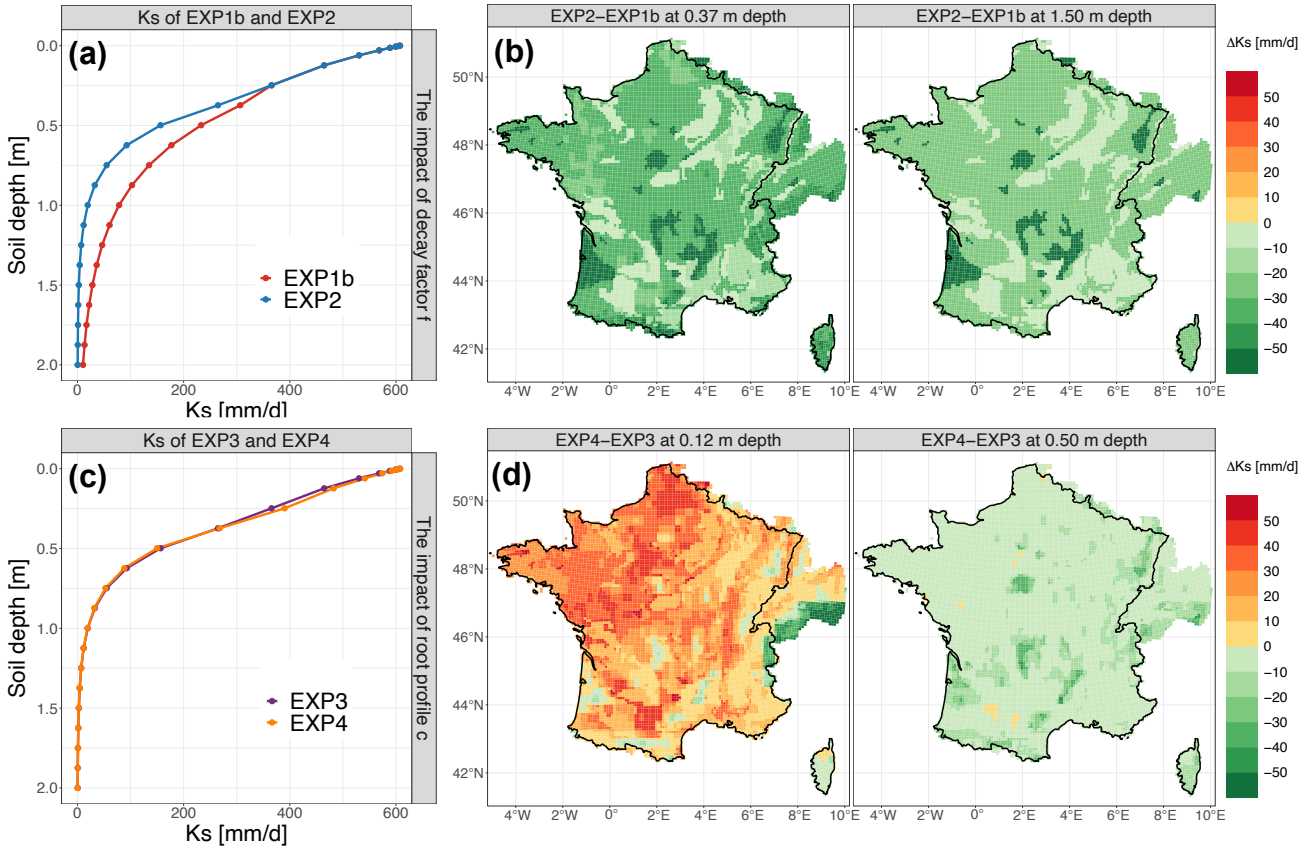

Figure S6. The simulated hydraulic conductivity in all soil layers averaged over France for the comparison between EXP1b and EXP2 (a) and the comparison between EXP3 and EXP4 (c). The difference in the simulated hydraulic conductivity between EXP1b and EXP2 (b) and between EXP3 and EXP4 (d) in some soil layers in France.

S5 Calibration of the soil water stress for transpiration

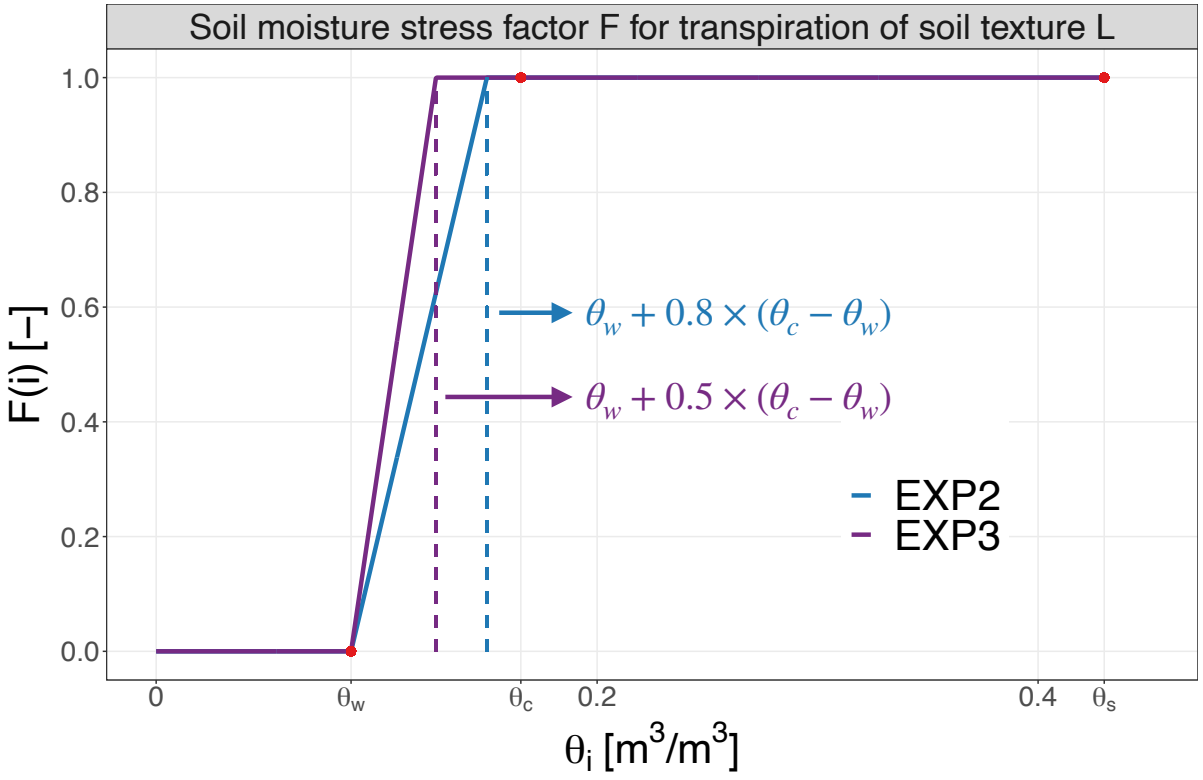

Figure S7. An example of the loamy soil texture (L) at soil depth layer i to show how soil moisture linearly constrains transpiration for calibration experiments EXP2 and EXP3. The water retention properties of the loamy soil texture are sourced from Table S2. When the soil moisture stress factor F is 0, transpiration is 0, and when F is 1, it reaches a maximum. F is 1 when the soil moisture is above $\theta_w + p \times (\theta_c - \theta_w)$ with p equal to 0.8 for EXP2 and 0.5 for EXP3.

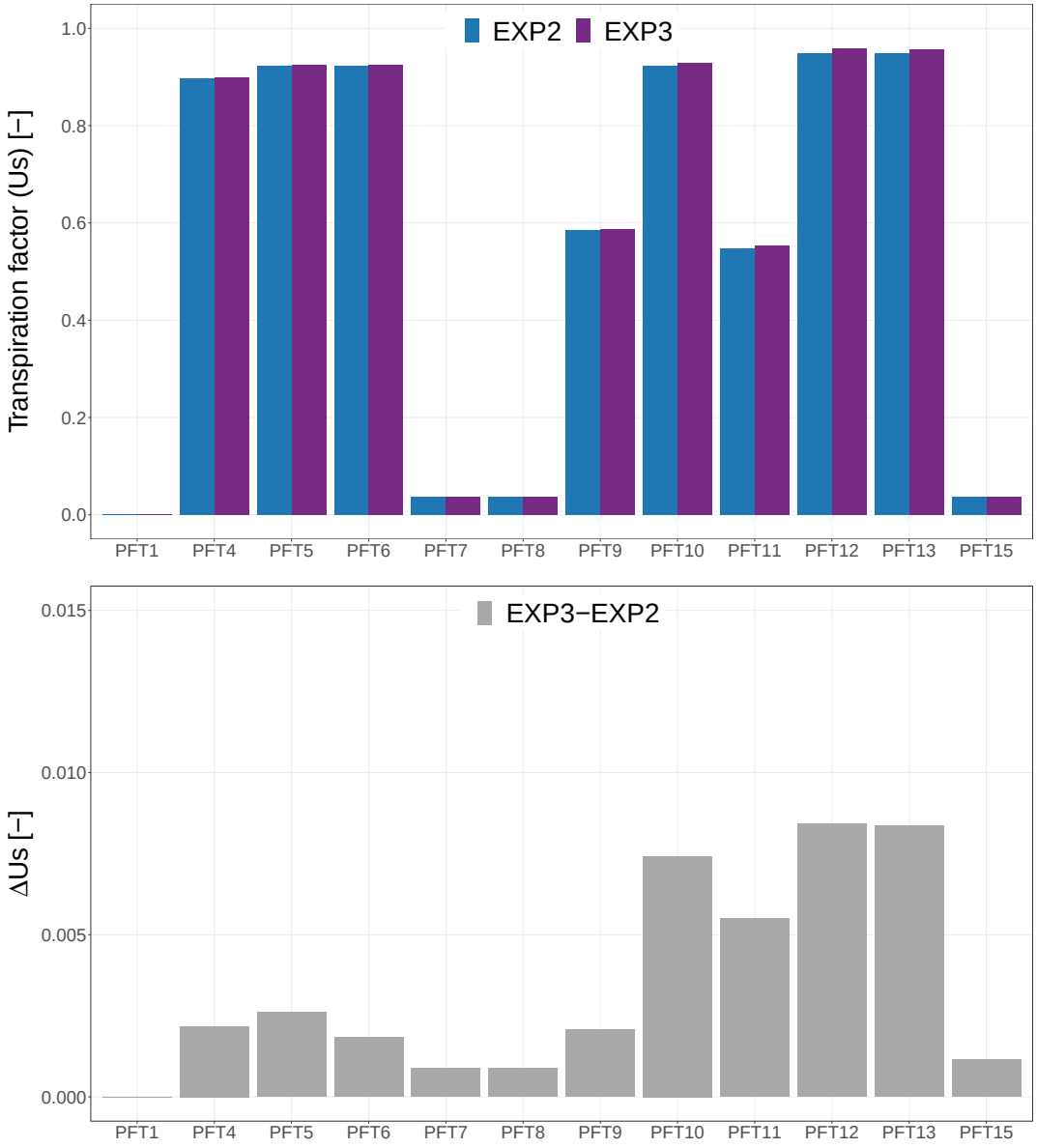

Figure S8. The transpiration factor (Us) at the PFT level averaged over France and the 1959-2020 period for the calibration experiments EXP2 and EXP3 in the top, and the difference in the bottom.

S6 Calibration of root density

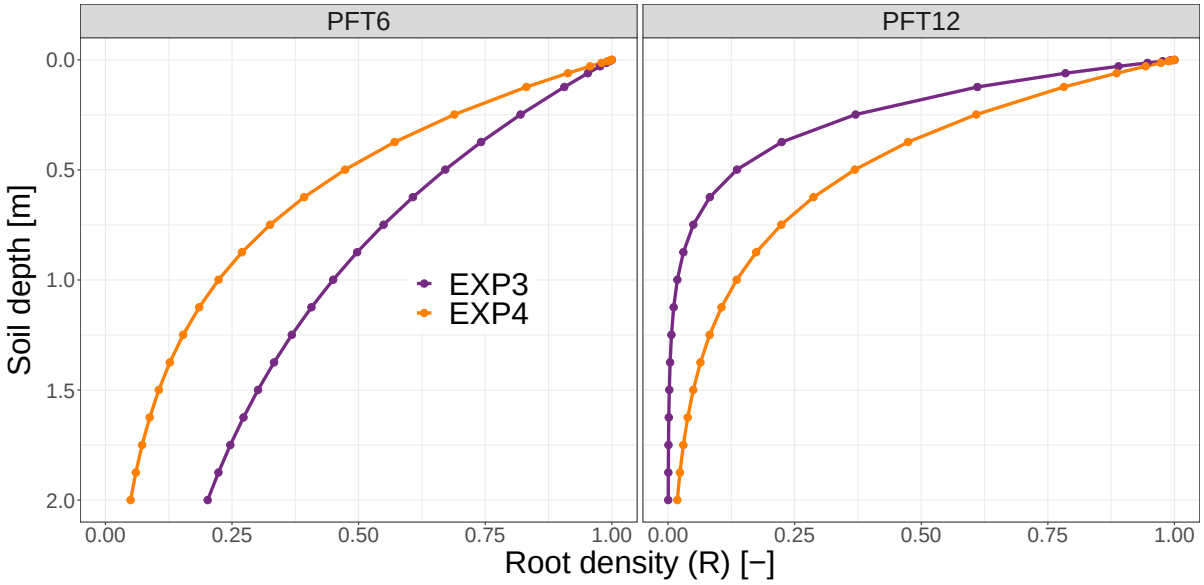

Figure S9. Two examples, PFTs 6 and 12, are used to show how root density changes with soil depth for calibration experiments EXP3 and EXP4.

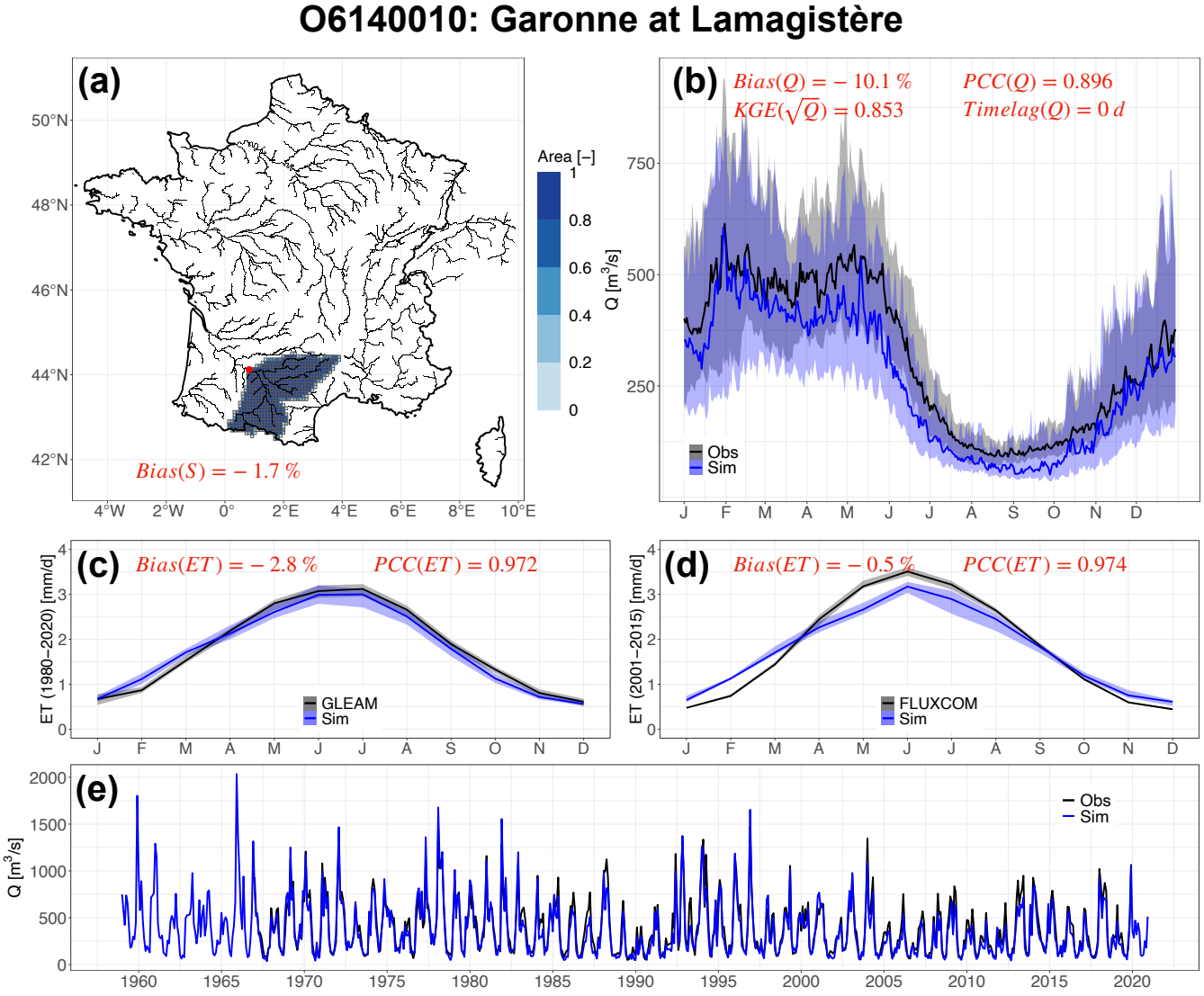

Figure S10. The same as in Figure 6 but for the Garonne River at the hydrometric station Lamagistère (O6140010).

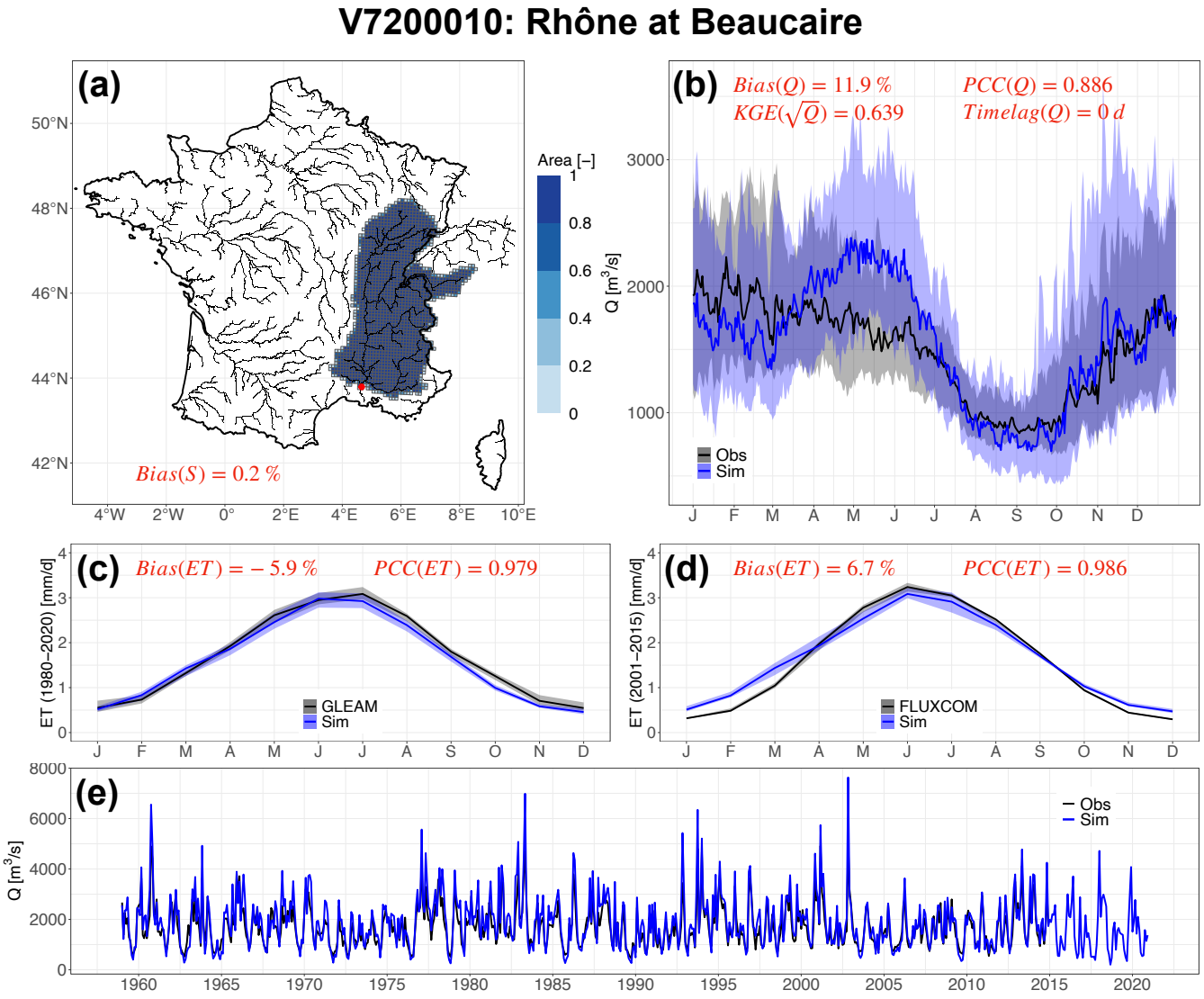

Figure S11. The same as in Figure 6 but for the Rhône River at the hydrometric station Beaucaire (V7200010).

S8 The simulated trends of water fluxes for several large river basins

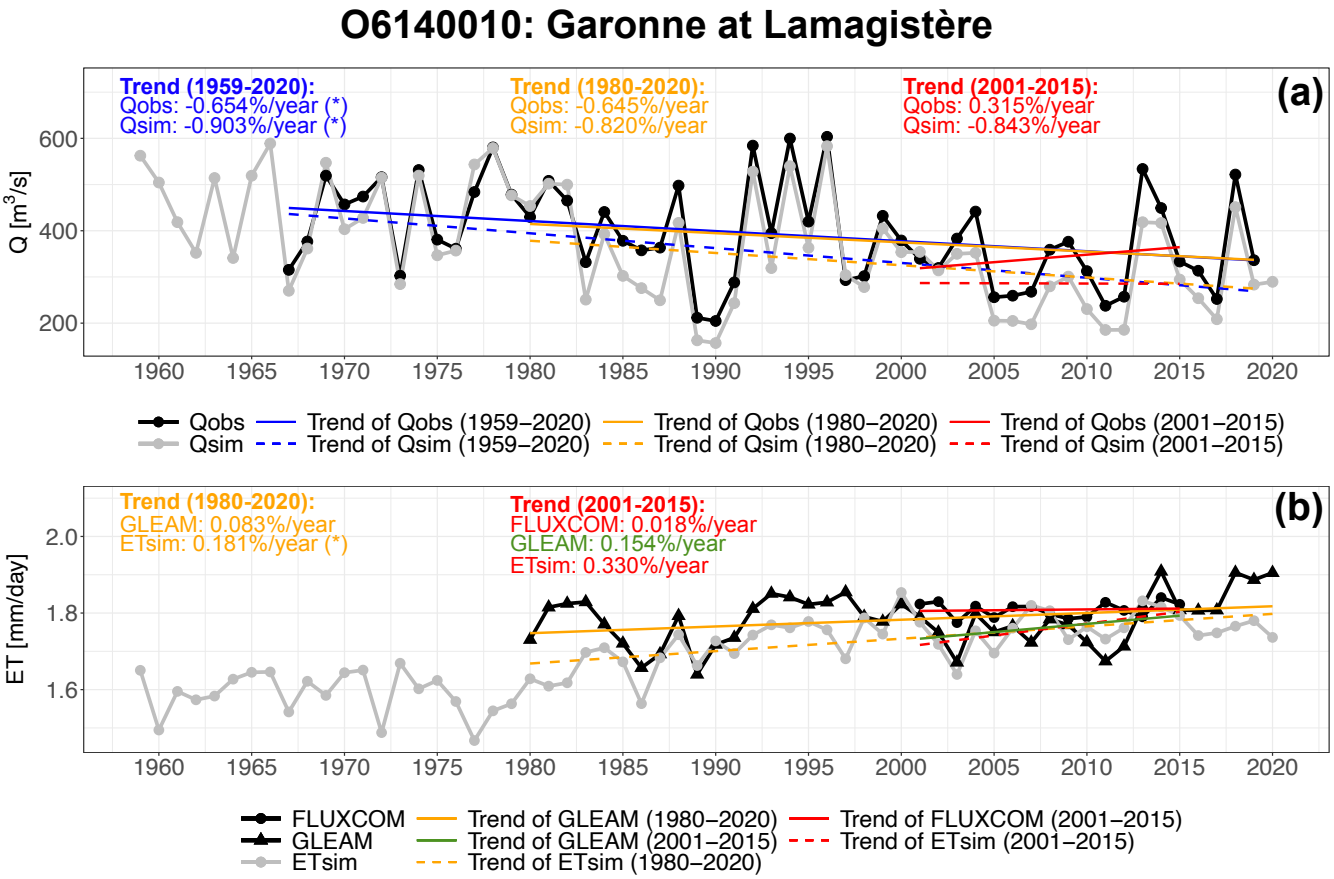

Figure S12. The same as in Figure 9 but for the Garonne River at the hydrometric station Lamagistère (O6140010).

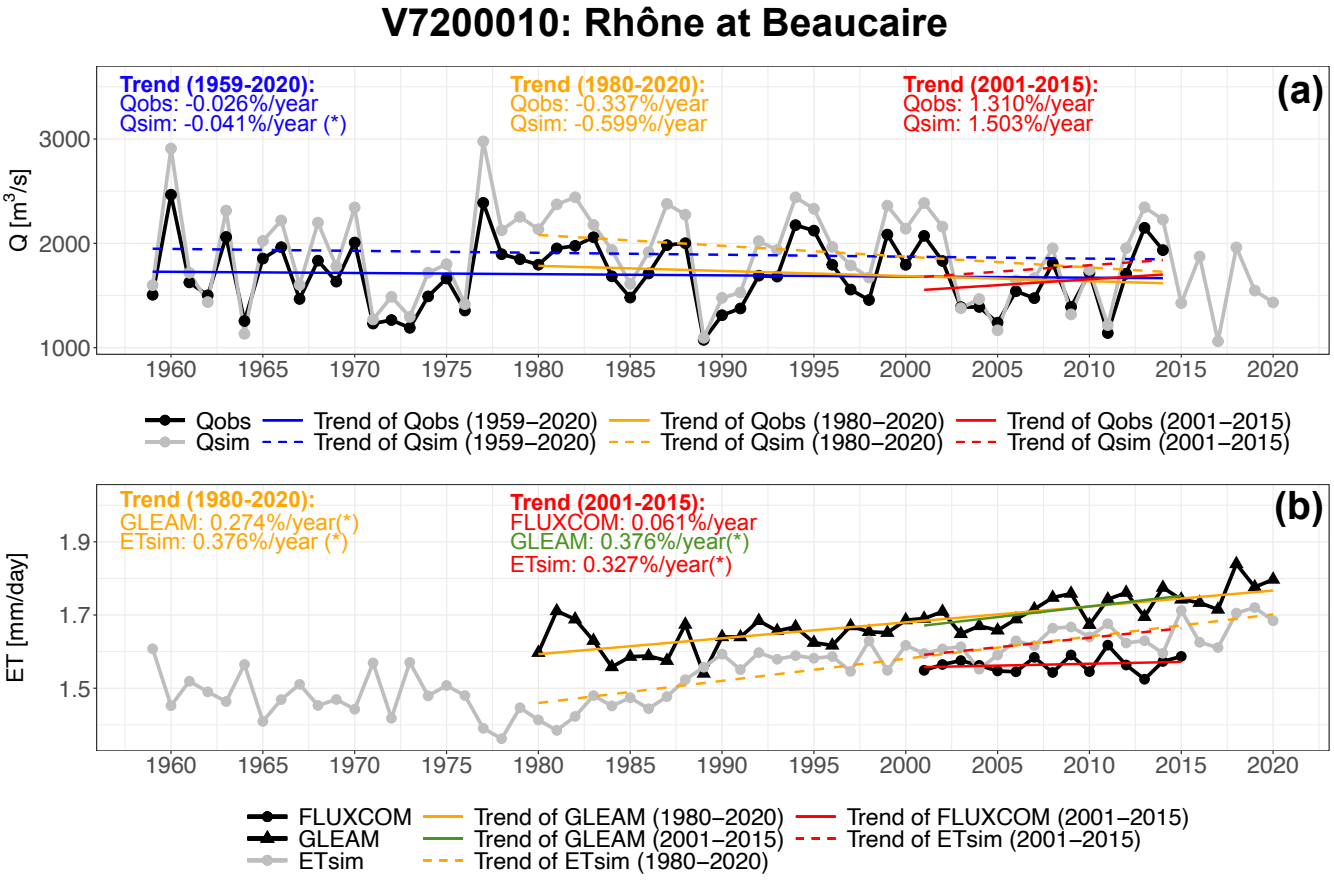

Figure S13. The same as in Figure 9 but for the Rhône River at the hydrometric station Beaucaire (V7200010).

S9 Human impacts on the simulated Q performance

Within the framework of the Explore2 project, the identification of human impacts on French river basins was based on the procedure of cross-referencing the Q observations from HydroPortail and possible sources of human activities on natural water resources. These sources are the French national BNPE dataset (https://bnpe.eaufrance.fr) that records water withdrawals as well as their uses for all the communes in France, and the AQUASTAT dataset (www.fao.org/aquastat/en/databases/dams that contains descriptive data (location, volume, and function) for 113 large dams over France. In addition, several indicators are calculated to quantify the human impacts on water resources: the ratio of upstream reservoir volume to naturalized annual Q, the ratio of summer withdrawals to naturalized summer Q, and the ratio of annual withdrawals to naturalized annual Q. The values of these indicators for natural or weakly influenced basins should be less than 5%, 10%, and 5%, respectively. The basins that do not meet the criteria are identified as influenced. Figure S14 shows that ORCHIDEE simulates Q better for the natural or weakly influenced basins than the influenced basins.

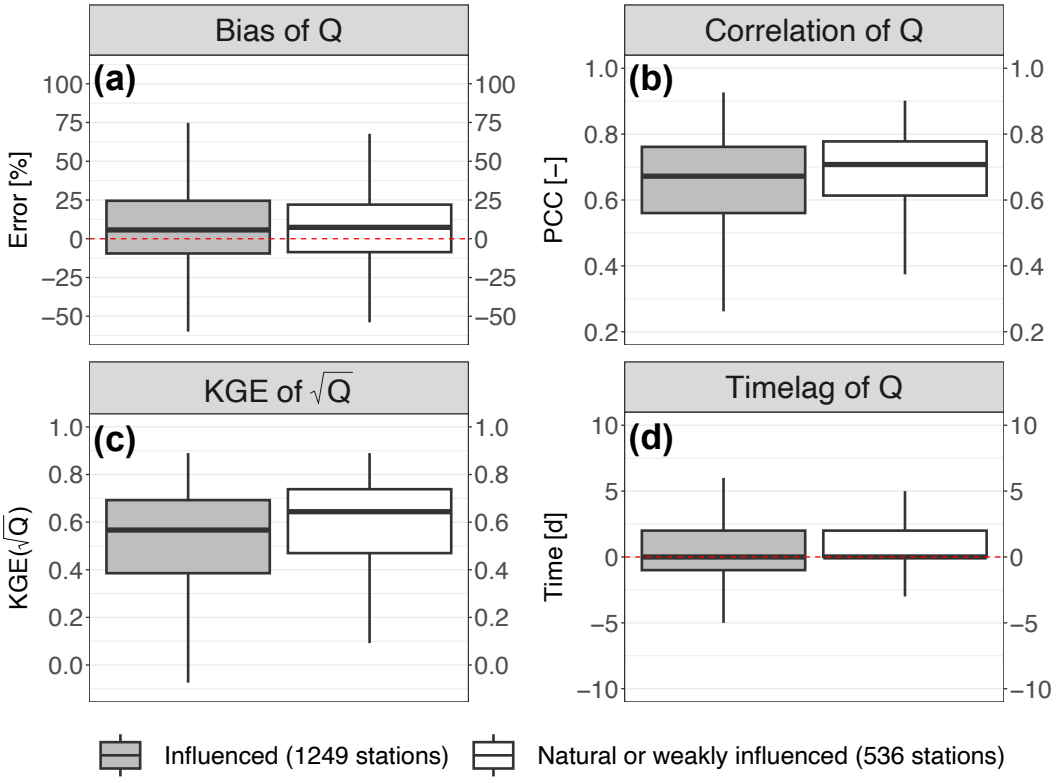

Figure S14. Performance criteria of the simulated Q in EXP4 for the influenced basins compared to the natural or weakly influenced basins: (a) bias; (b) Pearson correlation coefficient; (c) KGE of square-rooted simulated Q; (d) time lag.

S10 The sensitivity of Q performance to the length of evaluation period

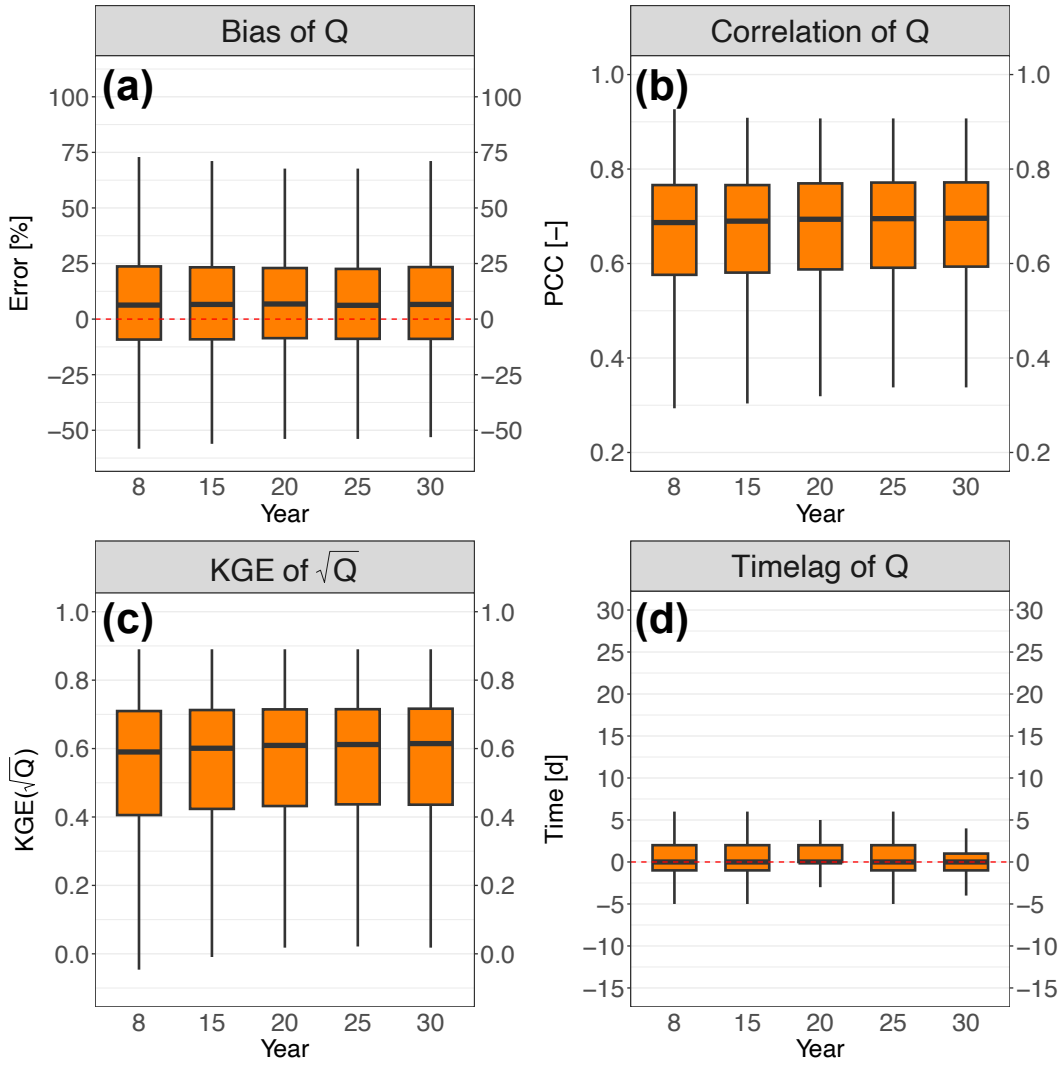

Figure S15. Performance criteria of the simulated Q in EXP4 calculated with the stations with different period length: (a) bias; (b) Pearson correlation coefficient; (c) KGE of square-rooted simulated Q; (d) time lag.

Table S3. The accuracy of the trend signal and trend significance of the simulated Q in EXP4 calculated with the stations with different period length.

Period length	8	15	20	25	30
Number of stations	1785	1477	1306	1106	969
Proportion to 1785 stations [%]	100	83	73	62	54
Trend signal accuracy [%]	76.4	76.0	76.0	76.7	78.3
Trend significance accuracy [%]	62.7	61.9	61.0	60.6	60.9

S11 Split sample tests on Q simulations

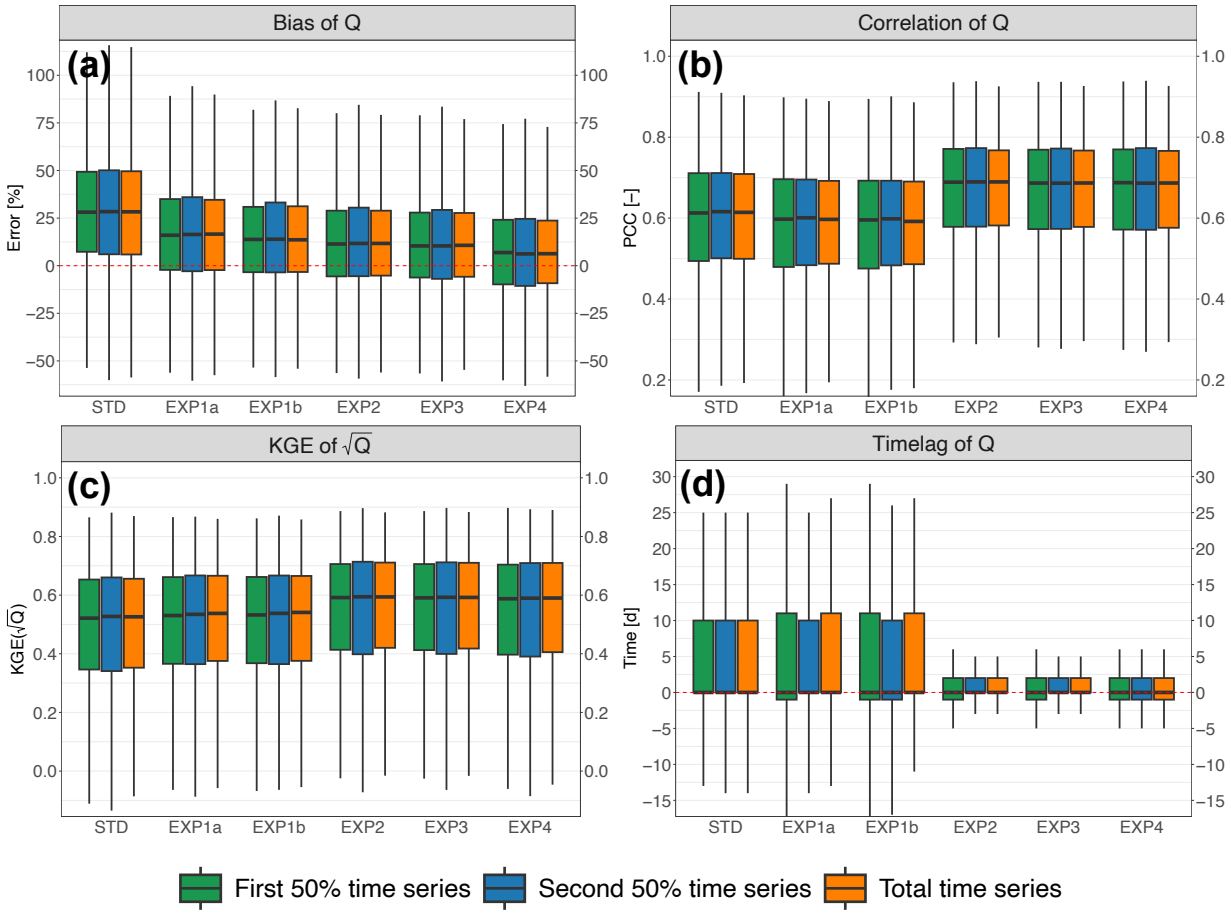

Figure S16. Split sample tests on the Q simulation performance criteria for the 6 calibration experiments with 3 separate periods (first half of Q time series, second half of Q time series and total Q time series): (a) bias; (b) Pearson correlation coefficient; (c) KGE of square-rooted simulated Q; (d) time lag.

References

Hurtt, G. C., Chini, L., Sahajpal, R., Frolking, S., Bodirsky, B. L., Calvin, K., Doelman, J. C., Fisk, J., Fujimori, S., Klein Goldewijk, K., Hasegawa, T., Havlik, P., Heinimann, A., Humpenöder, F., Jungclaus, J., Kaplan, J. O., Kennedy, J., Krisztin, T., Lawrence, D., Lawrence, P., Ma, L., Mertz, O., Pongratz, J., Popp, A., Poulter, B., Riahi, K., Shevliakova, E., Stehfest, E., Thornton, P., Tubiello, F. N., van Vuuren, D. P., and Zhang, X.: Harmonization of global land use change and management for the period 850–2100 (LUH2) for CMIP6, Geoscientific Model Development, 13, 5425–5464, https://doi.org/10.5194/gmd-13-5425-2020, 2020.

Reynolds, C. A., Jackson, T. J., and Rawls, W. J.: Estimating soil water-holding capacities by linking the Food and Agriculture Organization Soil map of the world with global pedon databases and continuous pedotransfer functions, Water Resources Research, 36, 3653–3662, https://doi.org/10.1029/2000WR900130, 2000.